X-Ray Investigation of Possible Super-Eddington Accretion in a Radio-loud Quasar at $z = 6.13$

Luca Ighina[1,2] , Alessandro Caccianiga[2] , Thomas Connor[1] , Alberto Moretti[2] , Fabio Pacucci[1,3] , Cormac Reynolds[4] ,
José Afonso[5,6] , Bruno Arsioli[5,6] , Silvia Belladitta[7,8] , Jess W. Broderick[4,9] , Daniele Dallacasa[10,11] , Roberto Della Ceca[2] ,
Francesco Haardt[12,13,14] , Erini Lambrides[15] , James K. Leung[16,17,18] , Alessandro Lupi[8,14,19] , Israel Matute[5,6] ,
Fabio Rigamonti[13,14,19] , Paola Severgnini[2] , Nick Seymour[9] , Fabrizio Tavecchio[13] , and Cristian Vignali[8,10]
[1] Center for Astrophysics—Harvard & Smithsonian, 60 Garden Street, Cambridge, MA 02138, USA; luca.ighina@cfa.harvard.edu
[2] INAF, Osservatorio Astronomico di Brera, via Brera 28, 20121, Milano, Italy
[3] Black Hole Initiative, Harvard University, 20 Garden Street, Cambridge, MA 02138, USA
[4] SKA Observatory, Science Operations Centre, CSIRO ARRC, 26 Dick Perry Avenue, Kensington, WA 6151, Australia
[5] Instituto de Astrofísica e Ciências do Espaço, Universidade de Lisboa, OAL, Tapada da Ajuda, Lisboa, Portugal
[6] Departamento de Física, Faculdade de Ciências, Universidade de Lisboa, Lisbon, Portugal
[7] Max Planck Institut für Astronomie, Königstuhl 17, D-69117 Heidelberg, Germany
[8] INAF—Osservatorio di Astrofisica e Scienza dello Spazio di Bologna, Via Gobetti 93/3, I-40129 Bologna, Italy
[9] International Centre for Radio Astronomy Research, Curtin University, 1 Turner Avenue, Bentley, WA 6102, Australia
[10] Dipartimento di Fisica e Astronomia "Augusto Righi," Università degli Studi di Bologna, Via Gobetti 93/2, 40129 Bologna, Italy
[11] INAF—Istituto di Radioastronomia, Via Gobetti 101, I-40129 Bologna, Italy
[12] Dipartimento di Scienza e Alta Tecnologia, Università degli Studi dell'Insubria, via Valleggio 11, I-22100 Como, Italy
[13] INAF, Osservatorio Astronomico di Brera, Via E. Bianchi 46, I-23807 Merate, Italy
[14] INFN, Sezione Milano-Bicocca, P.za della Scienza 3, I-20126 Milano, Italy
[15] NASA Goddard Space Flight Center, Code 662, Greenbelt, MD 20771, USA
[16] David A. Dunlap Department of Astronomy and Astrophysics, University of Toronto, 50 St. George Street, Toronto, ON M5S 3H4, Canada
[17] Dunlap Institute for Astronomy and Astrophysics, University of Toronto, 50 St. George Street, Toronto, ON M5S 3H4, Canada
[18] Racah Institute of Physics, The Hebrew University of Jerusalem, Jerusalem 91904, Israel
[19] Como Lake Center for Astrophysics, DiSAT, Università degli Studi dell'Insubria, via Valleggio 11, I-22100, Como, Italy

Abstract

We present radio and X-ray observations of the recently discovered $z = 6.13$ radio-powerful quasar RACS J032021.44−352104.1 using the upgraded Giant Metrewave Radio Telescope, the Australia Telescope Compact Array, the Australian Large Baseline Array, and Chandra. The observed radio properties are in line with what is typically observed in high-z radio quasars ($\alpha_r = 0.72 \pm 0.02$ and $L_{1.4\,\mathrm{GHz}} = 5.8 \pm 0.9 \times 10^{26}$ W Hz^{-1}). Despite the relatively low X-ray flux observed, $F_{0.5-7.0\,\mathrm{keV}} = 2.3 \pm 0.5 \times 10^{-14}$ erg s^{-1} cm^{-2}, the intrinsic luminosity in the 2–10 keV rest frame is markedly high, $L_{2-10\,\mathrm{keV}} = 1.8^{+1.1}_{-0.7} \times 10^{46}$ erg s^{-1}, making RACS J032021.44 −352104.1 one of the most luminous quasars currently known at $z > 5.5$. The high X-ray luminosity is largely driven by an extrapolation to energies below the observable X-ray window with Chandra and the slope derived in the 0.5–7 keV band (or 3.5–50 keV in the rest frame; $\Gamma_X = 3.3 \pm 0.4$). By analyzing the overall spectral energy distribution of the quasar, we found that the remarkably soft X-ray emission (1) cannot be produced by relativistic jets, even when relativistic boosting is considered, and (2) is consistent with expectations for a super-Eddington accreting supermassive black hole. If such a high accretion rate was confirmed, this source would be a unique laboratory to study high accretion in the early Universe and could help resolve some challenges inherent in early black hole growth paradigms.

1. Introduction

The observation of supermassive black holes (SMBHs; $M_{\mathrm{BH}} \gtrsim 10^8\,M_\odot$) hosted in $z \gtrsim 6$ quasars (e.g., F. Wang et al. 2021b) is one of the most important ways to constrain the initial mass of their seed black hole (BH). While there are several theoretical models predicting the formation of the first seed BHs (e.g., M. Volonteri & M. C. Begelman 2010; M. Volonteri et al. 2021), in order to explain the SMBHs we observe at $z \gtrsim 6$, models producing very massive seeds

($M_{\mathrm{seed}} \gtrsim 10^4\,M_\odot$) at $z \sim 15$ and accreting close to their Eddington limit[20] are favored (e.g., Á. Bogdán et al. 2024). However, these models typically require very rare and unique physical conditions (A. T. P. Schauer et al. 2017; A. Lupi et al. 2021; M. A. Latif et al. 2022) and struggle to explain the large abundances of $\sim 10^9\,M_\odot$ high-z quasars observed (X. Shen et al. 2020; X. Fan et al. 2023). Another way to reconcile theory with observations is to consider accretion above the Eddington limit, as shown in many simulations (A. K. Bhowmick et al. 2022; W. Massonneau et al. 2023; A. Lupi et al. 2024a). At the same time, it has been recently

---

[20] The Eddington limit for the accretion onto a BH of mass M_{BH} with radiative accretion efficiency ϵ is $\dot{M}_{\mathrm{Edd}} \approx 2.2 M_{\mathrm{BH}} \epsilon^{-1} \times 10^{-9}$ yr^{-1}. Super-Eddington accretion is when $\lambda_{\mathrm{Edd}} = \dot{M}/\dot{M}_{\mathrm{Edd}} > 1$.
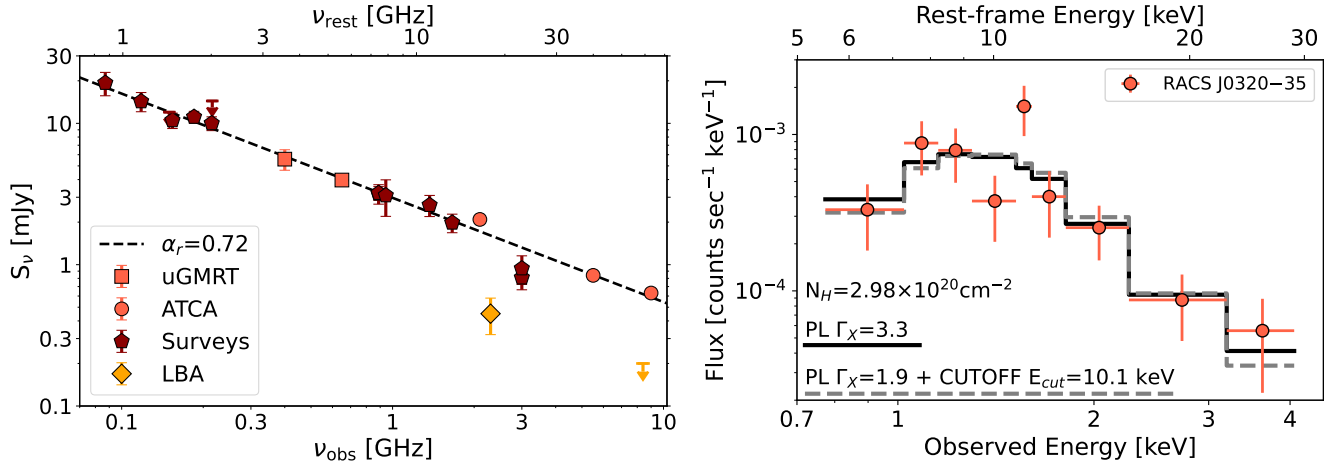
Figure 1. Left: radio spectrum of RACS J0320−35 obtained from dedicated observations (uGMRT+ATCA; light red squares and circles) as well as data available from public surveys (dark red pentagons), as described in the text. Measurements from the VAST survey are shown as a single data point at the median value (3.2 mJy beam^{-1}) and the standard deviation (0.5 mJy beam^{-1}) as uncertainty. The best-fit power law is shown as a black dashed line. We also show the measurement and upper limit from the VLBI-LBA observations (yellow diamond); as these observations are of significantly higher angular resolution, they were not used during the fit. Right: X-ray spectra of RACS J0320−35 obtained with Chandra. The best-fit power law with Galactic absorption is shown as a black solid line, while the best-fit power law ($\Gamma_{\rm X} = 1.9$, fixed) with an exponential cutoff and Galactic absorption is shown as a gray dashed line. Photon counts have been rebinned to 5σ for plotting purposes only.

suggested that super-Eddington accretion can also explain the observational properties (namely, the X-ray nondetection; e.g., R. Maiolino et al. 2024; M. Yue et al. 2024) of the new population of active galactic nuclei (AGN) revealed by the James Webb Space Telescope (JWST; see, e.g., E. Lambrides et al. 2024; P. Madau & F. Haardt 2024; F. Pacucci & R. Narayan 2024). Nevertheless, observational evidence for super-Eddington accretion has only been found for a handful of sources at high redshift (e.g., J. Wolf et al. 2023; R. Abuter et al. 2024) and suggested for some quasars in the epoch of reionization (J. Yang et al. 2021; L. Zappacosta et al. 2023; S. Belladitta et al. 2025). For example, H. Suh et al. (2025) recently reported the detection of an X-ray-luminous $\sim 7 \times 10^6 \, M_\odot$ BH at redshift $z \sim 4$. Based on the large X-ray and bolometric luminosity ($L_{\rm bol} \sim 10^{46.7}$ erg s^{-1}), the authors suggest that this system is accreting ~ 40 times its Eddington limit.

However, the vast majority of the $z > 6$ UV-bright quasar population has accretion rates consistent with being Eddington-limited (e.g., Y. Shen et al. 2019; E. P. Farina et al. 2022; C. Mazzucchelli et al. 2023). We must stress that these values are based on somewhat uncertain BH mass estimates (typically based on single-epoch measurements). Indeed, it has been shown how the BH mass of these very high-redshift systems can be overestimated by up to an order of magnitude, which in turn underestimates the accretion rates and implies that the need for very massive seed BHs is less severe (see, e.g., A. King 2024; E. Lambrides et al. 2024; A. Lupi et al. 2024b).

In this Letter, we present radio and X-ray observations of RACS J032021.44−352104.1 (hereafter RACS J0320−35) that suggest that the SMBH hosted in this system is accreting at a super-Eddington rate. This radio quasar belongs to a larger sample (see L. Ighina et al. 2025) selected from the combination of the first data release of the Rapid ASKAP Continuum Survey (RACS; D. McConnell et al. 2020; C. L. Hale et al. 2021) together with the Dark Energy Survey (DES; T. M. C. Abbott et al. 2021). RACS J0320−35 was then confirmed to be at $z = 6.13$ (based on the Lyman break) with the Gemini-South telescope (L. Ighina et al. 2023).

Throughout the Letter, we report spectral power-law slopes following the convention $S_\nu \propto \nu^{-\alpha}$, and all errors are reported at a 68% confidence level, unless otherwise specified. Throughout this work, we adopt a flat ΛCDM cosmology of $H_0 = 70$ km s^{-1}, $\Omega_{\rm M} = 0.3$, and $\Omega_\Lambda = 0.7$.

2. Radio and X-Ray Observations

Dedicated radio observations for RACS J0320−35 were obtained with the upgraded Giant Metrewave Radio Telescope (uGMRT; at 400 and 650 MHz), the Australia Telescope Compact Array (ATCA; at 2.1, 5.5, and 9.0 GHz), and the Australian Long Baseline Array (LBA; 2.4 and 8.4 GHz). We report in Appendix A a description of the observations, the steps of the data reduction, and the final images and fluxes obtained. Together with public data available from radio surveys (see Appendix A), we were able to constrain the radio emission of the quasar over the ~ 0.1–10 GHz observed frame (or 0.7–70 GHz in the rest frame) on arcsecond scales. At the same time, the LBA observations provide an estimate and an upper limit on the milliarcsecond emission at at 2.3 and 8.4 GHz, respectively.

We show in the left panel of Figure 1 the radio spectrum of RACS J0320−35. The spectral index obtained from a single power-law fit to the flux density measurements on arcsecond scales is $\alpha_{\rm r} = 0.72 \pm 0.02$. Although observations are separated across 6 yr (2019–2025), we do not find evidence for variation. Indeed, the reduced χ^2 parameter derived from the 28 measurements from the Australian Square Kilometre Array Pathfinder (ASKAP) as part of the Variables and Slow Transients (VAST; T. Murphy et al. 2013, 2021) survey at 888 MHz with a constant model is $\chi^2_{\rm red} = 0.83$. Similarly, the median peak flux density in these images ($S_{\rm 888\,MHz} = 3.2$ mJy beam^{-1}) is consistent with the estimate from the first scan of the RACS-low survey ($S_{\rm 888\,MHz} = 3.2$ mJy beam^{-1}), despite being taken about 6 yr apart in the observed frame. Moreover, fitting a radio power law solely in individual epochs (GLEAM-X, 2020 October; uGMRT, 2022 April; ATCA, 2022 September), the slope and normalization remain consistent with the single power-law fit. These findings suggest that, if present, variability does not

significantly affect the overall shape of the spectrum. However, monitoring on a larger time window is needed to constrain the variation on timescales of years in the rest frame.

The target appears pointlike on arcsecond scales based on a 2D Gaussian fit to the uGMRT and ATCA images. However, the flux recovered at 2.3 GHz on milliarcsecond scales with the LBA (0.45 ± 0.13 mJy) is only ∼20%–30% of the total flux recovered at larger scales (2.09 mJy at 2.1 GHz measured with ATCA or 1.61 mJy at 2.3 GHz from the best-fit power law). Similarly, at 8.4 GHz, the emission produced on milliarcsecond scales is <30% of the total flux density recovered on arcsecond scales. Although no significant variation was found on arcsecond scales, variability might still be present on the smaller scales.

In the X-rays, we observed RACS J0320−35 for 60 ks with the Advanced CCD Imaging Spectrometer (G. P. Garmire et al. 2003) on Chandra as part of Proposal 24700061 (PI: Ighina). A description of the observations and the data reduction is reported in Appendix B.1. In Figure 1, right panel, we show the best-fit model obtained from the fit of a power law absorbed by the Galactic column density ($N_H = 2.98 \times 10^{20}$ cm^{-2}; HI4PI Collaboration et al. 2016).

To fit the observed emission, we adopted two models, both of which include absorption by the Galactic column density ($N_H = 2.98 \times 10^{20}$ cm^{-2}; HI4PI Collaboration et al. 2016): single power, as typically adopted in the literature (e.g., T. Connor et al. 2021a; J.-T. Li et al. 2021), and a power law with an exponential cutoff, expected at low energies for highly accreting BHs (see discussion in Section 4.2 and, e.g., A. Tortosa et al. 2022). By considering a single power, we derived a very soft and luminous X-ray emission ($\Gamma_X = 3.3 \pm 0.7$ and $L_{2-10\,keV} = 1.8^{+2.2}_{-0.9} \times 10^{46}$ erg s^{-1}, errors at 90% confidence level) even in comparison to the optical ($\alpha_{ox} = 0.97 \pm 0.07$ errors at 90% confidence level; see L. Ighina et al. 2023 for the 2500Å luminosity).[21] The corresponding observed flux is $f_{0.5-7.0keV} = 2.3^{+1.1}_{-0.5} \times 10^{-14}$ erg s^{-1} cm^{-2} (errors at 90% confidence level).

If we consider a power law with a high-energy exponential cutoff where the photon index of the power law and the energy of the cutoff are both free to vary, the fit does not converge. Therefore, following the approach of A. Tortosa et al. (2024), we fixed the value of the photon index to $\Gamma_X = 1.9$ and estimated a cutoff energy of $E_{cut} = 10.1^{+10.7}_{-3.7}$ (errors at 90% confidence level). The corresponding luminosity and flux are $L_{2-10\,keV} = 0.9 \pm 0.3 \times 10^{46}$ erg s^{-1} and $f_{0.5-7.0keV} = 1.8^{+0.3}_{-0.2} \times 10^{-14}$ erg s^{-1} cm^{-2}, respectively (errors at 90% confidence level). In the case of a power law with a photon index fixed to $\Gamma_X = 2.2$, the corresponding energy cutoff, luminosity, and flux are $E_{cut} = 13.0^{+24.8}_{-5.5}$, $L_{2-10\,keV} = 1.0 \pm 0.3 \times 10^{46}$ erg s^{-1}, and $f_{0.5-7.0\,keV} = 1.9 \pm 0.3 \times 10^{-14}$ erg s^{-1} cm^{-2}, respectively (errors at 90% confidence level). In the following, we consider the best-fit single power law for the comparison of RACS J0320−35 to other high-z quasars, since most of the luminosities in the literature were computed with this model.

Finally, as a reference, we also report the values of flux and luminosity by assuming $\Gamma_X = 2$, which is often adopted in the literature for sources without meaningful constraints on the photon index (see, e.g., Z. Zuo et al. 2024). In this way, we obtained a luminosity that is about an order of magnitude

fainter compared to the best-fit photon index, with $L^{\Gamma_X=2}_{2-10\,keV} = 1.6 \times 10^{45}$ erg s^{-1}, even though the corresponding observed flux is only a factor of ∼3 lower ($f^{\Gamma_X=2}_{0.5-7.0\,keV} = 7.5 \times 10^{-15}$ erg s^{-1} cm^{-2}). This difference is mainly due to the extrapolation to energies not directly sampled with Chandra, which make the luminosity estimate highly dependent on the photon index value. As highlighted in the next section, many more objects at high redshift covered with relatively shallow observations might have a similar soft X-ray emission, and the assumption of $\Gamma_X = 2$ can systematically underestimate their luminosities.

3. Comparison with $z > 5.5$ Quasars

Based on the X-ray analysis of the Chandra observations of RACS J0320−35, its X-ray luminosity in the canonical 2–10 keV energy range is among the brightest ones observed in high-z quasars, even when considering sources with jets aligned close to our line of sight (i.e., blazars; see L. Ighina et al. 2019). In the left panel of Figure 2, we compare the rest-frame 2–10 keV X-ray luminosity of RACS J0320−35 to other known $z > 5.5$ quasars with dedicated Chandra or XMM-Newton X-ray observations from the literature. As is clear from the plot, RACS J0320−35 is among the X-ray-brightest sources in this redshift range, with an X-ray luminosity about ∼15 times higher than the median of all the X-ray-detected quasars, $\bar{L}_{2-10\,keV} \sim 1.3 \times 10^{45}$ erg s^{-1}. The only two sources with a comparable luminosity at $z > 6$ are PSO J030947 +271757108 at $z = 6.1$ (blue pentagons; S. Belladitta et al. 2020; A. Moretti et al. 2021) and CFHQS J142952+544717 at $z = 6.19$ (yellow triangles; C. J. Willott et al. 2010; G. Migliori et al. 2023; L. Marcotulli et al. 2025), while a third radio quasar with a similar luminosity ($L_{2-10\,keV} = 1.7$–3.6×10^{46} erg s^{-1}) is at $z = 5.47$ (G. A. Khorunzhev et al. 2021).

Interestingly, even though both these $z > 6$ quasars and RACS J0320−35 are radio-loud, suggesting that they all host powerful relativistic jets (see S. Frey et al. 2011; C. Spingola et al. 2020), their multiwavelength properties are quite different. PSO J030947+271757108 was classified as a flat-spectrum radio quasar (FSRQ; i.e., a blazar) based on its bright radio and X-ray luminosity (see S. Belladitta et al. 2020; C. Spingola et al. 2020). This source presented a statistically significant variability in the soft X-rays, with an increase of the 0.5–2 keV flux of a factor of ∼3 in only ∼300 s in the rest frame (A. Moretti et al. 2021). Similarly, based on recent NuSTAR observations, CFHQS J142952+544717 also showed signs of variability, increasing its total flux by a factor of ∼2.6 over a timescale of ∼110 days in the observed frame (∼15 days at $z = 6.19$; see L. Marcotulli et al. 2025) with respect to previous e-ROSITA, XMM-Newton, and Chandra estimates (P. Medvedev et al. 2020, 2021; G. Migliori et al. 2023). In both cases, the authors argue that the variability (and therefore the X-ray emission) is produced by the relativistic jets. Indeed, to explain the short timescales of these variations, relativistic effects are needed, since they increase the time in the source's rest frame. However, in the case of RACS J0320−35, we do not detect any significant variability on a rest-frame timescale of ∼30 days (similar to CFHQS J142952+544717), as detailed in Appendix B, albeit further monitoring on larger timescales is needed to rule out the presence of X-ray variability in the source. Moreover, in both cases, the slope of the X-ray emission is significantly harder ($\Gamma_X = 1.7 \pm 0.2$ for PSO J030947+271757108 and

---

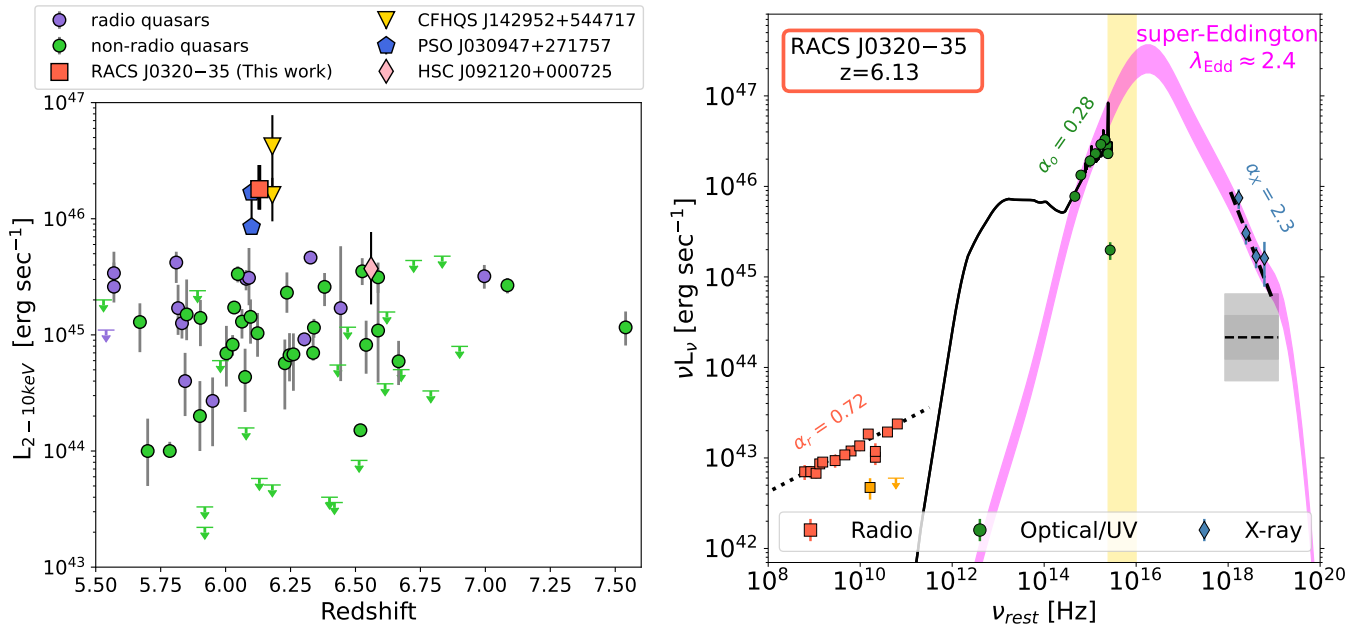[21] Where $\alpha_{ox} = 0.384 \log(L_{2\,keV}/L_{2500\,\text{Å}})$.

Figure 2. Left panel: X-ray luminosity in the 2–10 keV energy band (rest frame) as a function of redshift for the $z > 5.5$ quasars with X-ray observations from either Chandra or XMM-Newton available in the literature. We highlight the following objects: RACS J0320−35 (red square; this work), HSC J092120.56+000722.9 (pink diamond; J. Wolf et al. 2023), CFHQS J142952+544717 (yellow triangles; G. Migliori et al. 2023; L. Marcotulli et al. 2025), and PSO J030947+271757 (blue pentagons; A. Moretti et al. 2021). Since these last two sources present variable/flaring emission, we show two data points representing the quiescent and the flaring state, respectively. All the other quasars are reported with different colors based on whether they are also detected in the radio band (purple) or not (green). Right panel: rest-frame, multiwavelength SED of RACS J0320−35. The X-ray-weak super-Eddington SED from F. Pacucci & R. Narayan (2024) is shown in magenta. The solid black line is a quasar template (M. Polletta et al. 2007) matched to the optical–UV data points. The dashed black line is the X-ray emission expected from the UV–X-ray relation derived by E. Lusso & G. Risaliti (2016) and assuming $\Gamma_X = 2.0$. The gray regions show the 1σ and 2σ dispersion of the relation. The vertical yellow region indicates frequencies heavily affected by the absorption of the intergalactic medium.

$\Gamma_X = 2.2 \pm 0.2$ for CFHQS J142952+544717, errors at 90% confidence level; L. Ighina et al. 2022; G. Migliori et al. 2023) compared to RACS J0320−35 ($\Gamma_X = 3.3 \pm 0.4$). Indeed, not only is RACS J0320−35 one of the most X-ray-luminous quasars currently known at $z > 5.5$, it also presents a much larger photon index value compared to what is typically inferred for optically bright quasars—both radio-loud and radio-quiet—where Γ_X generally ranges from ∼1.8 to 2.0 (e.g., O. Shemmer et al. 2005, 2014; C. Vignali et al. 2005; A. Moretti et al. 2014; Y. Ai et al. 2017; R. Nanni et al. 2017; E. Bañados et al. 2018; F. Shaban et al. 2022). The only $z > 6$ source with a similar X-ray shape is HSC J092120+000722, a radio-quiet quasar at $z = 6.56$ (Y. Matsuoka et al. 2018). Based on dedicated Chandra observations, J. Wolf et al. (2023) derived an X-ray luminosity of $L_{2-10\,\text{keV}} = 3.7^{+4.0}_{-1.9} \times 10^{45}$ erg s^{-1}, consistent with other quasars at similar redshift (see pink diamond in Figure 2) but with an unusually steep photon index value, $\Gamma_X = 3.2^{+0.7}_{-0.6}$. Interestingly, using the Mg II broad emission line, J. Wolf et al. (2023) concluded that this system is hosting a ∼$2.5 \times 10^8\,M_\odot$ SMBH potentially accreting at a super-Eddington rate ($\lambda_{\text{Edd}} \approx 2.3$). As discussed in the next section, the large value of the photon index derived for this object (as for RACS J0320−35) is likely related to the high accretion rate.

However, we also stress that most of the X-ray observations currently available for $z > 5.5$ quasars are relatively shallow, and, due to the small number counts, they can only be used to estimate the observed flux. However, the slope of the X-ray emission remains unconstrained (see, e.g., F. Vito et al. 2019; L. Ighina et al. 2024). In these cases, a value of $\Gamma_X = 2$ is typically assumed when computing the rest-frame properties, which, however, would underestimate the $L_{2-10\,\text{keV}}$ luminosity if the emission was softer, as shown in the previous section for

RACS J0320−35. This also means that there might be many more quasars at high redshift with a similarly steep X-ray emission, potentially indicating that super-Eddington accretion is more common in the early Universe.

4. Origin of the X-Ray Emission

As discussed in the previous subsection, RACS J0320−35 stands out in terms of the intensity and shape of the X-ray emission when compared to the general quasar population, even at high redshift. For this reason, the origin of its high-energy emission is not easy to determine. Here we discuss different scenarios that could, in principle, reproduce the observed multiwavelength spectral energy distribution (SED) of RACS J0320−35 (shown in Figure 2, right panel).

4.1. Considering the Emission from the Relativistic Jets

Given the radio nature of RACS J0320−35, the X-ray luminosity of this source can be interpreted as due to the relativistically boosted radiation produced by jets oriented close to our line of sight—that is, the source is a blazar. Currently known high-z blazars belong to the FSRQ population and present both broad emission lines in the rest-frame UV spectrum as well as a strong and "hard" X-ray emission (or "flat" photon index, $\Gamma_X \lesssim 1.7$; L. Ighina et al. 2019; A. Moretti et al. 2021; E. Bañados et al. 2025). In these systems, the high-energy emission is normally interpreted as originating via inverse Compton (IC) interaction of the electrons within the jets with external seed photons produced by the accretion disk, the broad-line region (BLR), and/or the dusty torus (see, e.g., G. Ghisellini & F. Tavecchio 2009). While RACS J0320−35 also shows strong X-ray emission, the shape of its X-ray

spectrum is not consistent with the one expected from the IC interaction with external photons. At the same time, the IC interaction of the electrons with the low-frequency photons produced by the same electrons through a synchrotron process (Synchrotron-Self Compton interaction) would require a radio emission orders of magnitude larger than what is observed in RACS J0320−35.

The absence of the Lyα broad emission line (see L. Ighina et al. 2023) and the soft high-energy radiation could still be consistent with a BL Lac blazar nature, making it the most distant currently known in this class (e.g., V. S. Paliya et al. 2020a). These systems are characterized by very low accretion dominated by the advection of gas into the BH. This process makes the accretion less luminous compared to a typical geometrically thin and optically thick disk, resulting in a lower amount of ionizing photons and, consequently, of broad emission line intensity. At the same time, the continuum emission in the radio, optical, UV, and X-ray bands is dominated by the radiation produced by the jets after being amplified by relativistic boosting.

Based on the SED shape of RACS J0320−35, increasing in the optical/UV[22] and decreasing in the X-ray as a function of frequency ($\alpha_\nu^o = 0.28 \pm 0.03$; see L. Ighina et al. 2023), this source would be classified as a high synchrotron peaked blazar (HBL). In this case, the observed X-ray emission would be produced through a synchrotron process, as opposed to IC in the case of FSRQs (e.g., G. Ghisellini et al. 2013). The best-fit photon index derived for RACS J0320−35 ($\Gamma_X = 3.3 \pm 0.4$) would also be consistent with the ones typically observed in this HBL class ($\Gamma_X \sim 2–3$; see, e.g., R. Middei et al. 2022). Moreover, the X-ray-to-radio ratio[23] derived for RACS J0320−35 would be consistent with the typical values derived for the HBL population ($\alpha_{xr} = 0.51 \pm 0.03$; see, e.g., D. Donato et al. 2001), even though HBL sources are significantly fainter in both the radio and X-ray bands ($\log(\bar{L}_{5\,\mathrm{GHz}}\,\mathrm{erg}\,\mathrm{s}^{-1}) \sim 41.5$ and $\log(\bar{L}_{1\,\mathrm{keV}}\,\mathrm{erg}\,\mathrm{s}^{-1}) \sim 44.6$; D. Donato et al. 2001) with respect to RACS J0320−35 ($\log(L_{5\,\mathrm{GHz}}\,\mathrm{erg}\,\mathrm{s}^{-1}) \sim 43.0$ and $\log(L_{1\,\mathrm{keV}}\,\mathrm{erg}\,\mathrm{s}^{-1}) \sim 46.8$). Despite some similarities to HBL objects, there are several pieces of information that would rule out this nature. The radio properties of RACS J0320−35— namely, a relatively steep spectral index ($\alpha_r = 0.72 \pm 0.02$) and a faint core component on very long baseline inter-ferometry (VLBI) scales—suggest that its low-frequency emission is not dominated by relativistic beaming as expected for HBLs (e.g., Z. Wu et al. 2007; E. Liuzzo et al. 2013). Indeed, even if partially resolved, in HBL sources, we would still expect the core emission to dominate the flux density on milliarcsecond scales at the rest-frame frequencies sampled with the LBA ($\sim$15–60 GHz; see, e.g., B. G. Piner et al. 2010). Given the faint core emission, the overall radio emission observed in RACS J0320−35 is dominated by the extended regions of the relativistic jets, which are resolved in the LBA image (i.e., on scales $\gtrsim 50$ mas or $\gtrsim 300$ pc). This means the quasar is not a compact steep-spectrum or a peaked-spectrum radio source; that is, it is not a young radio object.

Moreover, its overall radio+optical/UV+X-ray SED can-not be reproduced by a single component (typically log

parabola; e.g., E. Massaro et al. 2004), as expected if they are all associated with the synchrotron emission of the relativistic jet (e.g., P. Giommi et al. 2021). We also checked γ-ray observations from the Fermi Large Area Telescope (LAT) but did not find any significant high-energy emission associated with the relativistic jets at the position of the quasar (see Appendix B.2). Finally, the absence of significant variability in the radio band on timescales of about 1 yr in the rest frame also disfavors an HBL nature for RACS J0320−35 (see, e.g., T. Hovatta et al. 2014), although monitoring in a larger time window is needed to properly characterize the presence/ absence of variability. Similarly, multiepoch monitoring in the optical–UV–X-ray rest-frame bands, where we expect HBL to be highly variable on timescales from days to years (e.g., Y.-H. Zhang & J.-C. Li 2017; A. Wierzcholska & S. Wagner 2025), will also be crucial to further rule out the BL Lac nature of RACS J0320−35. We stress that, if the HBL nature of RACS J0320−35 were confirmed, it would be, by far, the highest-redshift BL Lac blazar currently known (e.g., V. S. Paliya et al. 2020b).

4.2. Super-Eddington Accretion

Another possibility to explain the unique X-ray slope of RACS J0320−35 is the presence of an SMBH accreting above its Eddington limit.

Recently, there has been renewed interest in studying the X-ray properties of fast accretors because of a new population of high-z AGN uncovered by JWST at $z > 4$ that are not detected in X-rays (see, e.g., M. Yue et al. 2024; R. Maiolino et al. 2025). Several studies have investigated how super-Eddington accretion can naturally lead to an apparent X-ray weakness at high redshift, both from a theoretical perspective (K. Inayoshi et al. 2024; E. Lambrides et al. 2024; P. Madau & F. Haardt 2024) and through detailed simulations (e.g., F. Pacucci & R. Narayan 2024). In both cases, the X-ray nondetections are explained as due to a very steep X-ray emission that, when evaluated in the observed 0.5–7 keV energies (i.e., $\gtrsim$3–40 keV in the rest frame for $z \gtrsim 4$ sources), falls below the detection limit of current facilities.

From an observational point of view, evidence for a correlation between Γ_X and λ_{Edd} was found by several studies at low redshift (e.g., O. Shemmer et al. 2008; M. Brightman et al. 2013; R. Fanali et al. 2013). By analyzing the X-ray properties of highly accreting ($\lambda_{\mathrm{Edd}} > 0.8$) sources at $z \sim 0.1$–0.6, J. Huang et al. (2020) and H. Liu et al. (2021) found that the median photon index of these objects is larger ($\bar{\Gamma}_X = 2.2 \pm 0.2$) compared to sources with slower accretion ($\lambda_{\mathrm{Edd}} < 0.3$; $\bar{\Gamma}_X = 1.8 \pm 0.2$). Similarly, several studies targeting $z > 6$ UV-bright quasars revealed that they have a steeper photon index compared to $z < 6$ sources (see F. Vito et al. 2019; F. Wang et al. 2021a; L. Zappacosta et al. 2023). From the analysis of 18 highly accreting $z > 6$ quasars, L. Zappacosta et al. (2023) found the median photon index of these sources to be $\bar{\Gamma}_X = 2.4 \pm 0.1$, again significantly different from the $\Gamma_X = 1.8$–2.0 normally found at lower redshift. While some works interpreted this trend as an increase of the typical accretion rate of bright quasars as a function of redshift (e.g., G. Risaliti et al. 2009; F. Wang et al. 2021b), other works did not confirm the presence of a Γ_X–$\lambda_{\mathrm{Edd.}}$ relation (see, e.g., M. Laurenti et al. 2022; A. Tortosa et al. 2024).

---

[22] Based on data points from DES (T. M. C. Abbott et al. 2021), the VISTA Kilo-degree Infrared Galaxy (A. Edge et al. 2013), and the Wide-field Infrared Survey Explorer catalog (P. R. M. Eisenhardt et al. 2020).
[23] Quantified by $\alpha_{xr} = 0.13 \times \log(F_{1\,\mathrm{keV}}/F_{5\,\mathrm{GHz}})$, where the monochromatic fluxes are defined in the rest frame (G. Fossati et al. 1997).

In this context, the photon index value derived for RACS J0320−35 is larger, at more than a 95% confidence level, than all the super-Eddington sources analyzed by H. Liu et al. (2021) as well as the median value derived by L. Zappacosta et al. (2023). At the same time, the best-fit value derived for RACS J0320−35, $\Gamma_X = 3.3 \pm 0.4$, is fully consistent with the typical values derived from the simulation of $\lambda_{\rm Edd} \sim 2$–4 AGN described in F. Pacucci & R. Narayan (2024; median photon index of 3.1) as well as with the model proposed by P. Madau & F. Haardt (2024; expected photon index values $\gtrsim 2.8$). We stress that here the photon index value is simply a measurement of the soft-to-hard X-ray emission in this system, without the assumption of a physically motivated model. Indeed, in the case of super-Eddington accretion, we can expect the presence of a very low-energy cutoff ($E_{\rm cut} \sim 30$–40 keV; E. Kara et al. 2017; K. Inayoshi et al. 2024; P. Madau & F. Haardt 2024), which would also be consistent with the best-fit estimates derived in Section 2 ($E_{\rm cut} = 10.1^{+4.8}_{-2.6}$). Indeed, the combination of a very low-energy value for the cutoff and the high luminosity would put RACS J0320−35 in a unique place of the parameter space, compared to the general AGN population (see, e.g., Figure 4 in E. Bertola et al. 2022).

By making conservative assumptions on the bolometric luminosity of RACS J0320−35, we can have a rough estimate of the physical parameters of the accretion process. Given the optical and X-ray luminosity of RACS J0320−35, we can establish a minimum corresponding bolometric luminosity of $L \gtrsim 3 \times 10^{46}$ erg s^{-1}. The corresponding X-ray bolometric correction ($K_X = L_{\rm bol}/L_X$) is $K_X > 20$, based on the 1σ dispersion of the relation derived by F. Duras et al. (2020). At the same time, we can also assume that the BH hosted in RACS J0320−35 has mass $\lesssim 10^9 \, M_\odot$, based on SMBHs with similar optical/UV properties (e.g., C. Mazzucchelli et al. 2023). The corresponding Eddington ratio would be $\lambda_{\rm Edd} > 2.8$ (or $\lambda_{\rm Edd} > 1.4$ for the exponential cutoff model), supporting the super-Eddington accretion scenario. We note that these estimates do not take potential trends of the bolometric correction as a function of redshift (e.g., R. Maiolino et al. 2025) or Eddington ratio (e.g., K. K. Gupta et al. 2024) into account, which would further increase the derived value of $\lambda_{\rm Edd}$. Conversely, if we considered a BH accreting sub-Eddington, $\lambda_{\rm Edd} \sim 0.5$, the inferred BH mass would be $M_{\rm BH} \gtrsim 6 \times 10^9 \, M_\odot$—comparable to the most massive $z > 6$ SMBH yet known (e.g., X.-B. Wu et al. 2015) and with roughly 3 times the X-ray luminosity (T. Connor et al. 2021b).

Several models also predict different optical/UV properties in the case of super-Eddington accretion, in terms of both continuum (e.g., Q. Pognan et al. 2020) and emission lines (e.g., E. Lambrides et al. 2024). In particular, in the scenario proposed by P. Madau (2025), the strength of high-ionization emission lines depends on the viewing angle with respect to the rotation axis of the disk (see their Figure 7). Indeed, by assuming a disklike geometry for the BLR (e.g., C. M. Gaskell 2009; D. V. Savić et al. 2024; F. Rigamonti et al. 2025), the total UV continuum perceived by the BLR clouds and an observer with a different orientation can be very different. For the specific class of type 1 AGN—that is, observed close to the axis—the continuum emission produced by the disk outshines the line emission, resulting in apparent weak broad emission lines. As mentioned before, in the optical spectrum of RACS J0320−35 (L. Ighina et al. 2023), the Lyα line was not detected, broadly consistent with the scenario described in P. Madau (2025). However, the Lyα profile can also be affected by the absorption of neutral hydrogen; therefore, further near-infrared (NIR) observations covering additional emission lines are needed to test these predictions.

To visually compare the SED expected from a super-Eddington quasar and the observations obtained for RACS J0320−35, we considered the SEDs presented in F. Pacucci & R. Narayan (2024). In particular, these authors used general relativistic radiation magnetohydrodynamic (GRRMHD; see F. Pacucci & R. Narayan 2024 for details about the codes used) simulations of BHs with mass $M_{\rm BH} = 10^7 \, M_\odot$ accreting at super-Eddington rates up to $\lambda_{\rm Edd} = 13.4$ to compute the resulting SEDs. The study finds that the observed X-ray emission for mildly super-Eddington accretion ($1.4 < \lambda_{\rm Edd} < 4$) can be extremely steep, with a median photon index of $\Gamma_X = 3.1$ and a mode of $\Gamma_X = 4.4$, especially in slowly spinning or nonspinning BHs ($a \sim 0$)[24] observed at inclination angles greater than $30°$ from the polar axis. Based on these simulations, the nondetection of the $\sim 10^7 \, M_\odot$ SMBHs observed with JWST is due to the steep X-ray emission resulting in a faint emission at high energies, which are redshifted to the observed band.

We show in the right panel of Figure 2 the expected optical–UV–X-ray SED based on the results F. Pacucci & R. Narayan (2024). This SED is appropriate for a nonspinning ($a = 0$) SMBH accreting with $\lambda_{\rm Edd} = 2.4$; the emission is observed from an inclination of $i = 10°$ from the polar axis (see Figure 4, top left panel, in F. Pacucci & R. Narayan 2024). We stress that the simulations presented in F. Pacucci & R. Narayan (2024) focused on $\sim 10^7 \, M_\odot$ BHs and resulted in lower UV and X-ray luminosities. For this reason, we rescaled the SED obtained from the simulations to match the measurements of RACS J0320−35 (i.e., by a factor of ≈ 100). This normalization can be explained, by a first-order approximation, by a larger-mass SMBH ($\sim 10^9 \, M_\odot$, or even larger for $i > 10°$), as expected for RACS J0320−35. As shown in Figure 2, there is an excellent agreement between the expected emission and the observed data across the different wavelength bands. In particular, the quantitative properties in terms of relative UV-to-X-ray emission and shape of the simulated SED in F. Pacucci & R. Narayan (2024) considered here match closely those measured for RACS J0320−35: $\alpha_{\rm ox} = 0.99$ and $\Gamma_X = 3.14$.

We note that the presence of radio-bright jets in RACS J0320−35 would suggest larger values of the spin parameter compared to the one considered for the SED shown in Figure 2. While the comparison in Figure 2 is only meant to show the broad consistency between the quasars and the simulations of F. Pacucci & R. Narayan (2024), we also note that most of the radio emission is produced by extended regions of the jets (see Section 2), that is, related to previous activity of the SMBH, while the X-ray emission is measuring the more recent accretion process. Therefore, the SMBH could have slowed down due to the energy extracted by the relativistic jets themselves and decreased the value of a. Based on Equation (7) in D. L. Meier (2002), the e-folding spin-down timescale for a BH accreting at its Eddington limit and with a jet duty cycle of 10% is $\approx 2 \times 10^5$ yr. By assuming that the radio jet in RACS J0320−35 expanded with a $0.1c$

---

[24] Where a is the nondimensional spin parameter, which varies between 0, i.e., nonspinning, and 1, i.e., maximally spinning.

velocity (e.g., T. An & W. A. Baan 2012) up to $\approx 0.''3–1''$ (or $\approx 1.7–5.6$ kpc; i.e., in between the ATCA and LBA resolutions), the associated jet activity timescale is $\approx 1–10 \times 10^5$ yr (for an inclination of $10°–30°$), that is, enough for the BH to significantly spin down. Using GRRMHD simulations, A. Ricarte et al. (2023) showed that for $10–10^4 \, M_\odot$ BHs, the equilibrium spin parameter in the presence of relativistic jets and mildly super-Eddington accretion lies between $a \sim 0.3$ and 0.6. Detailed simulations, similar to the ones presented in F. Pacucci & R. Narayan (2024), targeting a higher mass range of $\sim 10^{8–9} \, M_\odot$ for different spin values will be crucial to accurately constrain the properties of the SMBH hosted in RACS J0320−35.

5. Conclusions

In this work, we presented the multiwavelength properties of a recently discovered $z = 6.13$ radio-bright quasar, RACS J0320−35 (L. Ighina et al. 2023, 2025).

Based on dedicated uGMRT+ATCA observations, we concluded that the source presents a radio emission typical of the general radio-loud population ($\alpha_r = 0.72 \pm 0.02$; e.g., G. Calistro Rivera et al. 2017) and does not show signs of strong variability on timescales of ~ 6 yr in the observed frame. Dedicated VLBI-LBA observations revealed that the core radio emission (on ~ 20 mas scales) is faint, a factor of $\sim 3–5$ lower compared to the one observed on arcsecond scales. Finally, the overall radio+optical/NIR+X-ray SED cannot be reproduced by a single log-parabola component. Together, these observations suggest that the emission observed in RACS J0320−35 is not dominated by relativistic boosting—that is, RACS J0320−35 is not a blazar, albeit further multiepoch and multiwavelength observations are needed to fully discard this scenario.

While the low-energy properties of RACS J0320−35 are consistent with the typical radio-loud population of quasars, high-energy observations with the Chandra telescope uncovered an unusually strong and soft X-ray emission. In particular, RACS J0320−35 is, within the errors, the most X-ray-luminous quasar at $z > 5.5$ ($L_{2-10 \, keV} = 1.8^{+1.1}_{-0.7} \times 10^{46}$ erg s^{-1}) and the one with the steepest photon index ($\Gamma_X = 3.3 \pm 0.4$). At the same time, we also note that an accurate estimate of the photon index is not available for most of the high-z quasars currently detected in the X-rays. Therefore, deeper X-ray observations of a large sample of $z \gtrsim 6$ sources are necessary to test whether such soft X-ray emission is more common in the early Universe.

The most likely scenario that could explain the steep X-ray spectrum in RACS J0320−35 is that its SMBH is accreting above its Eddington limit. Indeed, the observed X-ray slope (or potential cutoff, depending on the model) is fully consistent with theoretical predictions describing super-Eddington accretion (e.g., K. Inayoshi et al. 2024; P. Madau & F. Haardt 2024). Moreover, we showed that the optical+UV+X-ray SED of RACS J0320−35 can be well reproduced by the presence of an SMBH with $M_{BH} \approx 10^9 \, M_\odot$ and $\lambda_{Edd} = 2.4$, based on the simulations and models presented in F. Pacucci & R. Narayan (2024).

The overall multiwavelength properties of RACS J0320−35 make it one of the most promising candidates for super-Eddington accretion in the early Universe. Many recent works on super-Eddington accretion focused on the AGN population uncovered by JWST. However, due to their low BH mass ($\sim 10^7 \, M_\odot$), these systems are much fainter, and only upper

limits are available in the X-rays (e.g., R. Maiolino et al. 2025). Given its high luminosity across the entire electromagnetic spectrum, RACS J0320−35 offers the perfect laboratory where we can directly test predictions of theoretical models and simulations in the context of super-Eddington accretion. To this end, future IR spectroscopic observations covering broad emission lines (e.g., C IV, Mg II, H$_\alpha$, and H$_\beta$) will be essential to constrain the mass and accretion properties of the SMBH hosted in RACS J0320−35 and confirm or discard the presence of super-Eddington accretion. At the same time, deeper X-ray observations will also be crucial to better constrain the X-ray intensity and shape, especially in the soft part of the spectrum, where we expect the majority of the X-ray emission.

Finally, the radio-bright nature of this unique quasar might imply an accretion–jets relation. For example, in the scenario proposed by E. J. D. Jolley & Z. Kuncic (2008), jets can enhance the accretion onto the central SMBH by converting part of the accreting mass energy into jet kinetic power instead of radiation, which otherwise generally limits further accretion. As relativistic jets carry away a substantial amount of kinetic power but very little mass, jetted quasars could, in principle, accrete more material than quasars with a similar UV luminosity but without relativistic jets (see, e.g., T. Connor et al. 2024).

Appendix A
Radio Observations and Analysis

In L. Ighina et al. (2023), we were only able to loosely constrain the radio emission observed in RACS J0320−35 based on the measurements and upper limits available from public surveys. To better characterize the spectral shape and the emission produced at different scales in this system, we performed dedicated observations with the uGMRT, ATCA, and LBA arrays. In this section, we describe these observations and the corresponding data reduction.

A.1. Survey Observations

RACS J0320−35 was covered as part of several public radio surveys in addition to the observations reported in L. Ighina et al. (2023; see their Table 3), namely, with the Murchison Widefield Array (MWA) and ASKAP. In particular, RACS J0320−35 is detected in the second data release of the GaLactic and Extra-Galactic All-sky MWA extended (GLEAM-X; K. Ross et al. 2024) survey, covering the 70–231 MHz frequency range. Here we consider the flux density measurements from the five wide bands of the GLEAM-X survey as reported in the catalog: 19.3 ± 3.5 at 87 MHz, 14.3 ± 2.1 at 118 MHz, 10.5 ± 1.2 at 154 MHz, 11.1 ± 0.9 at 185 MHz, and 10.0 ± 1.0 at 215 MHz. In Figure 3, we show the GLEAM-X image in the very wide band (170–231 MHz) centered on the optical position of RACS J0320−35. The quasar has also been detected in several scans of the RACS survey, including the third scan at low frequency ($S_{944 \, MHz} = 3.09 \pm 0.88$ mJy) and the first scans at mid ($S_{1.37 \, GHz} = 2.64 \pm 0.43$ mJy; S. W. Duchesne et al. 2023, 2024) and high ($S_{1.66 \, GHz} = 1.98 \pm 0.28$ mJy; S. W. Duchesne et al. 2025) frequencies. Finally, RACS J0320−35 belongs to the high decl. field of the VAST (T. Murphy et al. 2013, 2021) survey performed with ASKAP. RACS J0320−35 was covered a total of 28 times at 888 MHz between 2023 July and 2025 April. We estimated the peak flux density of RACS J0320−35 directly from the images, and we did not apply corrections to account for small differences in the flux scales of each epoch (e.g., D. McConnell et al. 2020). In Figure 4, we show the flux density of RACS J0320−35 at 888 MHz as a function of time. The average peak flux density of the source is $S_{888 \, MHz} = 3.2$ mJy beam^{-1}, and the standard deviation is 0.5 mJy beam^{-1}, consistent with the median rms
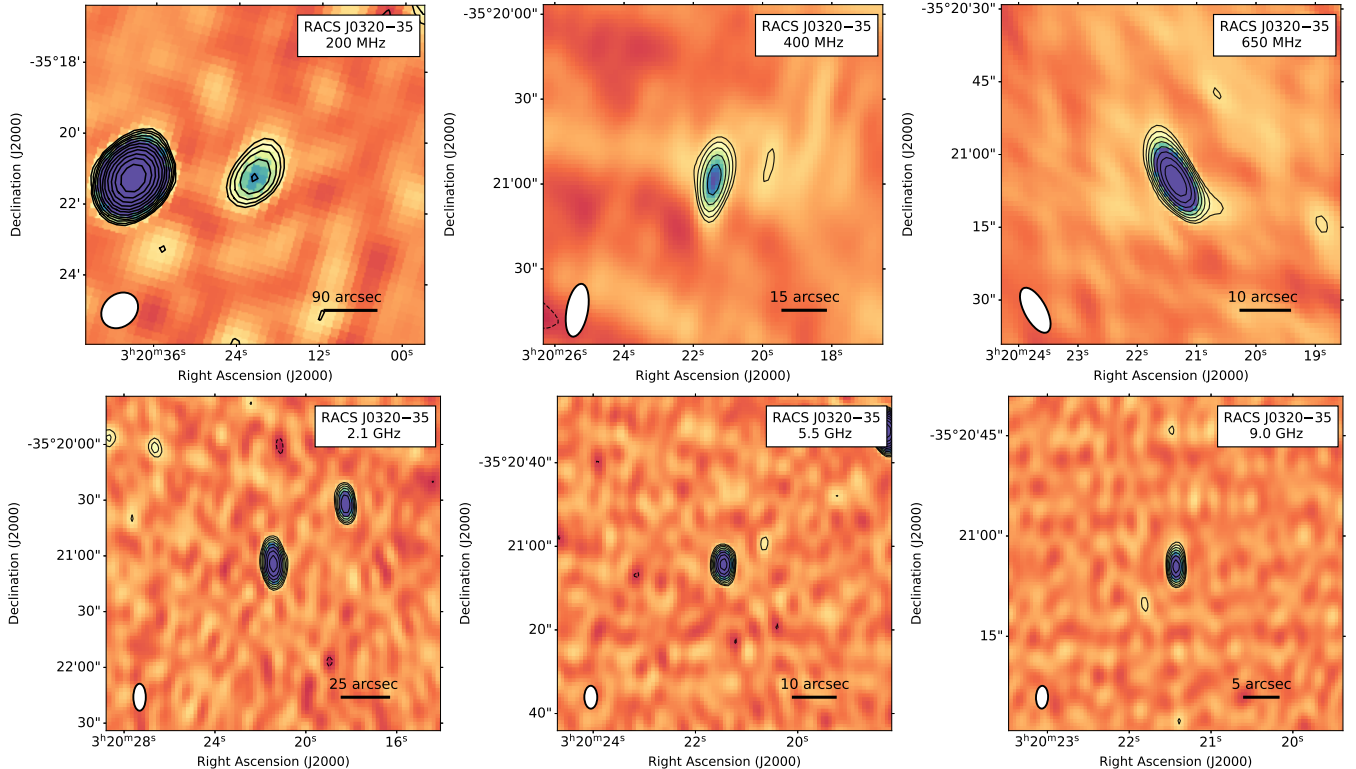

Figure 3. MWA (200 MHz), uGMRT (400 and 650 MHz), and ATCA (2.1, 5.5, and 9 GHz) images centered on the optical position of RACS J0320−35. Contours start at $\pm 3 \times$ rms and increase by factors of $\sqrt{2}$.
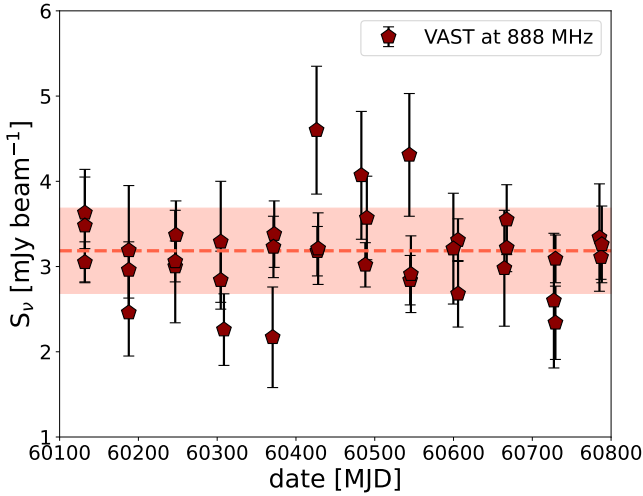
Figure 4. Light curve at 888 MHz, observed frame, of RACS J0320−35 based on the data from the VAST survey. Measurements span a range of ∼2 yr in the observed frame, from 2023 July to 2025 April. The dashed line is the weighted average, while the shaded area represents the 1σ standard deviation (=0.5 mJy beam^{-1}), comparable to the median uncertainty of the measurements (=0.4 mJy beam^{-1}).

(0.4 mJy beam^{-1}) and the typical uncertainty including epoch-to-epoch flux scale variations (∼0.5 mJy beam^{-1}; see Equation (7) in D. McConnell et al. 2020). To check for any potential signs of variability, we computed the modulation index parameter (V) and the reduced chi square ($\chi^2_{\rm red}$) with respect to a constant model (see Equations (1) and (2) in T. Murphy et al. 2021). For RACS J0320−35, we obtained: $V = 0.16$ and

$\chi^2_{\rm red} = 0.83$. Both these values suggests that the radio emission in the quasar is not significantly variable on timescales up to ∼2 yr. Moreover, we also note that the median values derived from VAST are fully consistent with the peak flux density measured from the first scan of RACS-low (performed on 2019 July) at 888 MHz ($S_{888\ \rm MHz} = 3.2 \pm 0.3$ mJy beam^{-1}). Once again, these measurements suggest no significant variation on timescales of ∼6 yr in the observed frame, or ∼1 in the rest frame, without accounting for potential beaming effects.

A.2. uGMRT Observations

uGMRT observations of RACS J0320−35 were performed on 2022 April 23 (project 42_001; PI: Ighina) using the GMRT wideband backend (S. H. Reddy et al. 2017 with a bandwidth of 200 MHz) in band 3 (centered at 400 MHz) and band 4 (centered at 650 MHz). During the run, we observed 3C 48 as a primary calibrator and 0409−179 as a secondary calibrator. The data reduction was performed using the CAsa Pipeline-cum-Toolkit for Upgraded GMRT data REduction (R. Kale & C. H. Ishwara-Chandra 2021) code by applying further flagging depending on the specific observation. For the imaging analysis, we adopted a robust parameter of 0.5, that is, a compromise between resolution and sensitivity. We report the images obtained in Figure 3 and the results of a 2D Gaussian fit using the Common Astronomy Software Applications package (CASA; J. P. McMullin et al. 2007) in Table 1. When fitting the radio spectrum, we also considered a conservative 10% (added in quadrature) in the errors to account for the uncertainty related to the calibration process.

Table 1
Best-fit Values Obtained from a 2D Gaussian Fit to the uGMRT and ATCA Images of RACS J0320−35

Array	Frequency (GHz)	Int. Flux (mJy)	Peak Surf. Brightness (mJy beam^{-1})	Beam Sizes (maj × min)	P.A. (deg)	Off-source rms (μJy beam^{-1})	Obs. Date Y–M–D
(1)	(2)	(3)	(4)	(5)	(6)	(7)	(8)
uGMRT	0.40	5.58 ± 0.88	5.17 ± 0.39	$18\rlap{.}''9 \times 7\rlap{.}''5$	-100.3	370	2022–04–23
uGMRT	0.65	3.97 ± 0.17	3.76 ± 0.08	$10\rlap{.}''3 \times 4\rlap{.}''5$	-61.4	80	2022–04–23
ATCA	2.1	2.09 ± 0.09	1.91 ± 0.05	$14\rlap{.}''5 \times 6\rlap{.}''7$	0.1	45	2022–09–03
ATCA	5.5	0.84 ± 0.03	0.87 ± 0.02	$5\rlap{.}''5 \times 3\rlap{.}''1$	0.5	19	2022–09–03
ATCA	9.0	0.63 ± 0.03	0.63 ± 0.02	$3\rlap{.}''4 \times 1\rlap{.}''8$	-1.9	19	2022–09–03
LBA	2.3	⋯	0.45 ± 0.13	25.7×18.3 mas	11.6	95	2022–10–21
LBA	8.4	⋯	<0.17	5.7×4.0 mas	16.6	55	2022–10–23

Note. Column (1): array used for a given observation. Column (2): central frequency of the observation. Column (3): integrated flux density. Column (4): peak surface brightness. Column (5): size of the synthesized beam in arcseconds. The LBA beams are in units of milliarcseconds. Column (6): position angle east of north of the synthesized beam. Column (7): rms of the image near the source. Column (8): date observations were performed.

A.3. ATCA Observations

Dedicated ATCA observations of RACS J0320−35 were performed on 2022 September 3 with the most extended 6D configuration under the project C3477 (PI: Ighina). However, antenna CA06 was not available, reducing the maximum baseline to ∼2500 m. Observations were carried out at 2.1, 5.5, and 9 GHz using the Compact Array Broadband Bandwidth (W. E. Wilson et al. 2011), with a nominal bandwidth of 2048 MHz (divided into channels of 1 MHz). We used the source PKS B1934−638 as the standard primary calibrator (J. Reynolds 1994), observed at the beginning of the session. To calibrate the phases throughout the session, we periodically observed 0402−362. The final on-source time (after flagging) for RACS J0320−35 is 1.7, 2.4, and 2.2 hr at 2.1, 5.5, and 9 GHz, respectively. To process the data (calibration and imaging), we used the MIRIAD data reduction package (R. J. Sault et al. 1995) following a standard reduction together with two cycles of phase self-calibration. For imaging, we adopted a standard robust parameter of 0.5, and the results are shown in Figure 3. Finally, we performed a 2D Gaussian fit on the target using the CASA software. The source is clearly detected and appears pointlike in all the observations. We report the results of the fit in Table 1. When fitting the radio spectrum, we also considered a conservative 10% (added in quadrature) in the errors to account for the uncertainty related to the calibration process.

A.4. VLBI-LBA Observations

VLBI observations of RACS J0320−35 were performed with the LBA (project v619; PI: Ighina) on 2022 October 21 (at 2.3 GHz) and 23 (at 8.4 GHz). Each observing run was 12 hr and included another target (as well as their calibrators and slewing time) plus 1 hr of setup and fringe finding. During the observations, we used 0332−375 for the phase referencing.

For both sessions, the ATCA, Mopra, Parkes, Ceduna, Katherine, Yarragadee, and Warkworth antennas were used. During the 8.4 GHz session, the Hobart antenna was also added to the array. However, all of the Yarragadee and Warkworth measurements were flagged at 2.3 GHz, whereas all of the Katherine measurements were flagged for the 8.4 GHz observations. The final longest baselines were 2611 and 5362 km at 2.3 and 8.4 GHz, respectively.

Data were processed using the NRAO's Astronomical Imaging Processing System (AIPS; D. C. Wells 1985), where the calibration and flagging followed the general procedure outlined in the AIPS cookbook. The accuracy of the flux scale is ∼20%. We considered this uncertainty, added in quadrature, when computing the errors on the fluxes measured from these images. For imaging, we adopted a weighting robust parameter equal to 2 in order to enhance the sensitivity at the expense of the angular resolution. The restored images obtained after cleaning (using the imagr task in AIPS) are reported in Figure 5. The final images reach an rms of ∼95 μJy beam^{-1} and ∼55 μJy beam^{-1} at 2.3 and 8.4 GHz, respectively.

At 2.3 GHz, a 5σ radio signal is present ∼16 mas away from the optical position of the quasar reported in the DES catalog (white cross in Figure 5). Even though the signal-to-noise ratio (S/N) of this radio emission alone is relatively low (S/N ∼ 5), the close position to the expected core is an indication that this emission is true and likely produced by the innermost regions of the jets, close to the accretion disk. Therefore, we considered its peak flux density ($S_{2.3\,\text{GHz}}^{\text{peak}} = 450 \pm 130$ μJy beam^{-1}) as an estimate of the radio emission produced within the core of RACS J0320−35. At 8.4 GHz, there is no significant radio signal at the target position or within a ∼200 mas radius around it. Therefore, using a 3σ upper limit at 8.4 GHz ($S_{8.4\,\text{GHz}} < 170$ μJy beam^{-1}), we can conclude that the radio core of the source RACS J0320−35 has a spectral index $\alpha_r^{\text{core}} \gtrsim 0.5$.
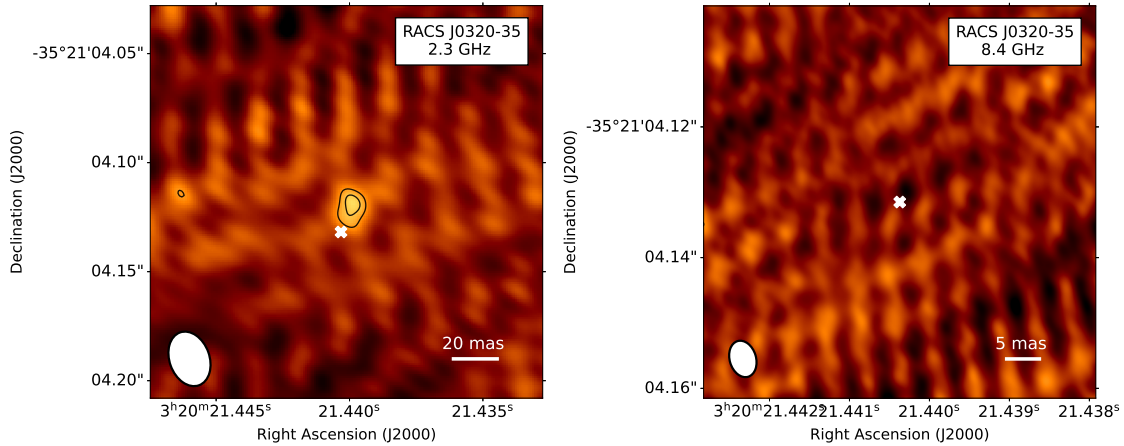

Figure 5. LBA-VLBI images of RACS J0320−35 centered at 2.3 (left) and 8.4 (right) GHz. The white cross shows the optical position of RACS J0320−35 from the DES catalog. Contours start at ±3× rms and increase by factors of $\sqrt{2}$.

Appendix B
High-energy Observations and Analysis

B.1. X-Ray Observations with Chandra

In this section, we describe the Chandra X-ray observations of RACS J0320−35. The overall exposure time, 60 ks, was split into two groupings, with one observation (27112; 29.68 ks) conducted in 2023 July and two observations (26709 and 29162; 15.87 and 14.74 ks, respectively) conducted in 2023 December; all observations are contained in the Chandra Data Collection 318 doi:10.25574/cdc.318. Events were recorded in the very faint telemetry format and timed exposure mode, with RACS J0320−35 positioned on the back-illuminated S3 chip. Data reduction was performed using the software CIAO (v4.16; A. Fruscione et al. 2006) with CALDB (v4.11.2). We show in Figure 6, left panel, the 0.5–7.0 keV image obtained from the combination of the different exposures. A relatively strong X-ray source is detected at the optical position of the quasar.

We used specextract to extract events from a 2″ source region and a background annulus of 10″–30″, both centered on the optical/NIR position of the quasar. The target is detected with 52 net counts over a background of ≲1 photon in the 0.5–7.0 keV energy band. We then analyzed the extracted spectra using XSPEC v12.11.1 (K. A. Arnaud 1996) and performed a

fit minimizing the modified C-statistic (W. Cash 1979; K. Wachter et al. 1979). We binned the spectrum to one net count per energy bin, and we limited the fit to the energy range of 0.5–7.0 keV. We considered two models: a simple power law absorbed by the Galactic column density along the line of sight (tbabs×pow) and a power law with an exponential cutoff at higher energies and Galactic absorption (tbabs×z-cutoffpl). In both cases, we fixed the column density to $N_H = 2.98 \times 10^{20}$ cm^{-2} (HI4PI Collaboration et al. 2016). For the power law with an exponential cutoff model, we fixed the value of the power-law photon index to $\Gamma_X = 1.9$ and 2.2 (e.g., A. Tortosa et al. 2024), since the fit would not converge with three free parameters. We report in Table 2 the best-fit parameters derived for each model.

In order to check for potential variability between the two observing epochs, we analyzed the 27112 and 26709+29162 (taken less than 1 day apart) observations separately. For this analysis, we adopted a single power-law fit. We show in Figure 6, right panel, the contours of the best fits of these observations. Contours represent the 68% and 90% confidence limits on the modified C-statistic. Within the uncertainties, both epochs are consistent with each other, indicating that there was no significant variation and that we can jointly fit the entire 60 ks.
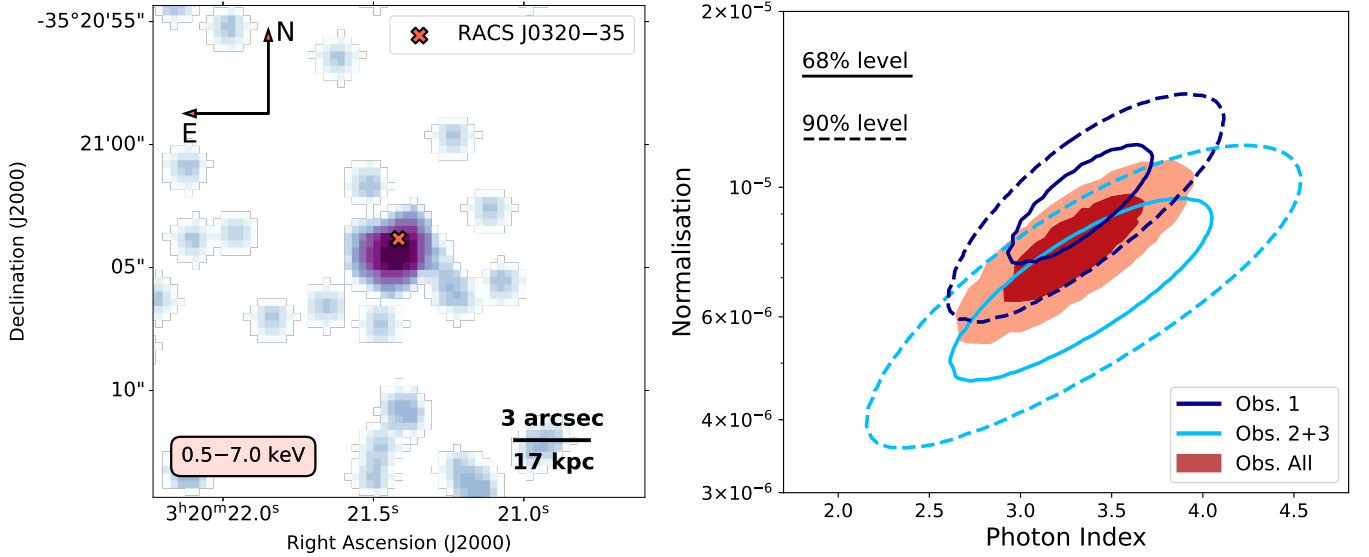

Figure 6. Left: Chandra images (20″ × 20″) of RACS J0320−35 in the energy band 0.5–7 keV. The red cross indicates the optical position of the quasar, consistent with the X-ray source detected in the Chandra image. Right: contour levels of the photon index and normalization parameter derived from the fit of the Chandra observations. Different colors indicate different observation segments, with the filled ellipses showing the contours from all the observations combined. Dashed (solid) lines indicate the 90% (68%) confidence regions.

Table 2
Best-fit Values Obtained from the Fit of the X-Ray Spectrum of RACS J0320−35

Model (1)	Γ_X (2)	E_{cut} (3)	$f_{0.5-7.0\ keV}$ (4)	$L_{2-10\ keV}$ (5)	α_{ox} (6)	C-stat/d.o.f. (7)
PL	3.3 ± 0.4	⋯	$2.3^{+0.5}_{-0.3}$	$1.8^{+1.1}_{-0.7}$	0.97 ± 0.05	35/43
PL+CUTOFF	1.9*	$10.1^{+4.8}_{-2.6}$	1.8 ± 0.1	0.9 ± 0.2	$1.19^{+0.06}_{-0.05}$	36/43
PL+CUTOFF	2.2*	$13.0^{+8.9}_{-4.0}$	$1.9^{+0.1}_{-0.2}$	$1.0^{+0.3}_{-0.2}$	$1.14^{+0.06}_{-0.05}$	36/43

Note. During the fit, we assumed a simple power law with Galactic absorption, and the errors are reported at a 68% confidence level. Column (2): photon index of the power law. Column (3): energy of the exponential cutoff. Column (4): unabsorbed flux in the energy band 0.5–7 keV in units of 10^{-14} erg s^{-1} cm^{-2}. Column (5): rest-frame luminosity in the energy range 2–10 keV in units of 10^{46} erg s^{-1}. Column (6): α_{ox} parameter. Column (7): C-statistic and degrees of freedom of the fit.
∗ An asterisk indicates a fixed value.

B.2. γ-Ray Upper Limits from Fermi-LAT

Since BL Lac, and blazars in general, are the main population of extragalactic γ-ray emitters (e.g., A. Konigl 1981), we also considered the data available from Fermi-LAT in the MeV–GeV energy regime. For the analysis, we followed the same setup described in B. Arsioli et al. (2025), integrating over 17 yr of observations with LAT, but considering a broader energy range, between 600 MeV and 800 GeV. No significant γ-ray emission was found; that is, the likelihood analysis resulted in test statistics (TS) of approximately zero, setting an upper limit flux of $\sim$2e-13 erg cm^{-2} s^{-1} at 1 GeV.[25] A complementary light-curve search with time bins of 100 days, aimed at unveiling flares that could be diluted in the long 17 yr exposure, returned no significant excess. The most pronounced interval reaches only TS $\sim$ 6, well below the 3σ detection threshold (TS $\geqslant$ 12) for this type of analysis. We therefore found no evidence, either persistent or transient, for γ-ray emission in RACS J0320−35.

ORCID iDs

Luca Ighina ● https://orcid.org/0000-0003-1516-9450
Alessandro Caccianiga ● https://orcid.org/0000-0002-2339-8264
Thomas Connor ● https://orcid.org/0000-0002-7898-7664
Alberto Moretti ● https://orcid.org/0000-0002-9770-0315
Fabio Pacucci ● https://orcid.org/0000-0001-9879-7780
Cormac Reynolds ● https://orcid.org/0000-0002-8978-0626
Bruno Arsioli ● https://orcid.org/0000-0001-8166-6602
Erini Lambrides ● https://orcid.org/0000-0003-3216-7190
Alessandro Lupi ● https://orcid.org/0000-0001-6106-7821
Paola Severgnini ● https://orcid.org/0000-0001-5619-5896
Nick Seymour ● https://orcid.org/0000-0003-3506-5536
Fabrizio Tavecchio ● https://orcid.org/0000-0003-0256-0995
Cristian Vignali ● https://orcid.org/0000-0002-8853-9611

References

Abbott, T. M. C., Adamów, M., Aguena, M., et al. 2021, ApJS, 255, 20
Abuter, R., Allouche, F., Amorim, A., et al. 2024, Natur, 627, 281
Ai, Y., Fabian, A. C., Fan, X., et al. 2017, MNRAS, 470, 1587
An, T., & Baan, W. A. 2012, ApJ, 760, 77
Arnaud, K. A. 1996, in ASP Conf. Ser. 101, Astronomical Data Analysis Software and Systems V, ed. G. H. Jacoby & J. Barnes (San Francisco, CA: ASP), 17
Arsioli, B., Chang, Y.-L., & Ighina, L. 2025, MNRAS, 539, 1458
Astropy Collaboration, Price-Whelan, A. M., Lim, P. L., et al. 2022, ApJ, 935, 167
Astropy Collaboration, Price-Whelan, A. M., Sipőcz, B. M., et al. 2018, AJ, 156, 123
Astropy Collaboration, Robitaille, T. P., Tollerud, E. J., et al. 2013, A&A, 558, A33
Bañados, E., Connor, T., Stern, D., et al. 2018, ApJL, 856, L25
Bañados, E., Momjian, E., Connor, T., et al. 2025, NatAs, 9, 293
Belladitta, S., Bañados, E., Xie, Z.-L., et al. 2025, arXiv:2505.15923
Belladitta, S., Moretti, A., Caccianiga, A., et al. 2020, A&A, 635, L7
Bertola, E., Vignali, C., Lanzuisi, G., et al. 2022, A&A, 662, A98
Bhowmick, A. K., Blecha, L., Ni, Y., et al. 2022, MNRAS, 516, 138
Bogdán, Á., Goulding, A. D., Natarajan, P., et al. 2024, NatAs, 8, 126
Brightman, M., Silverman, J. D., Mainieri, V., et al. 2013, MNRAS, 433, 2485
Calistro Rivera, G., Williams, W. L., Hardcastle, M. J., et al. 2017, MNRAS, 469, 3468
Cash, W. 1979, ApJ, 228, 939
Connor, T., Bañados, E., Cappelluti, N., & Foord, A. 2024, Univ, 10, 227
Connor, T., Bañados, E., Stern, D., et al. 2021a, ApJ, 911, 120

Connor, T., Stern, D., Bañados, E., & Mazzucchelli, C. 2021b, ApJL, 922, L24
Donato, D., Ghisellini, G., Tagliaferri, G., & Fossati, G. 2001, A&A, 375, 739
Duchesne, S. W., Grundy, J. A., Heald, G. H., et al. 2024, PASA, 41, e003
Duchesne, S. W., Ross, K., Thomson, A. J. M., et al. 2025, PASA, 42, e038
Duchesne, S. W., Thomson, A. J. M., Pritchard, J., et al. 2023, PASA, 40, e034
Duras, F., Bongiorno, A., Ricci, F., et al. 2020, A&A, 636, A73
Edge, A., Sutherland, W., Kuijken, K., et al. 2013, Msngr, 154, 32
Eisenhardt, P. R. M., Marocco, F., Fowler, J. W., et al. 2020, ApJS, 247, 69
Fan, X., Bañados, E., & Simcoe, R. A. 2023, ARA&A, 61, 373
Fanali, R., Caccianiga, A., Severgnini, P., et al. 2013, MNRAS, 433, 648
Farina, E. P., Schindler, J.-T., Walter, F., et al. 2022, ApJ, 941, 106
Fossati, G., Celotti, A., Ghisellini, G., & Maraschi, L. 1997, MNRAS, 289, 136
Frey, S., Paragi, Z., Gurvits, L. I., Gabányi, K. É., & Cseh, D. 2011, A&A, 531, L5
Fruscione, A., McDowell, J. C., Allen, G. E., et al. 2006, Proc. SPIE, 6270, 62701V
Garmire, G. P., Bautz, M. W., Ford, P. G., Nousek, J. A., & Ricker, G. R. J. 2003, Proc. SPIE, 4851, 28
Gaskell, C. M. 2009, NewAR, 53, 140
Ghisellini, G., Haardt, F., Della Ceca, R., Volonteri, M., & Sbarrato, T. 2013, MNRAS, 432, 2818
Ghisellini, G., & Tavecchio, F. 2009, MNRAS, 397, 985
Giommi, P., Perri, M., Capalbi, M., et al. 2021, MNRAS, 507, 5690
Gupta, K. K., Ricci, C., Temple, M. J., et al. 2024, A&A, 691, A203
Hale, C. L., McConnell, D., Thomson, A. J. M., et al. 2021, PASA, 38, e058
HI4PI Collaboration, Ben Bekhti, N., Flöer, L., et al. 2016, A&A, 594, A116
Hovatta, T., Pavlidou, V., King, O. G., et al. 2014, MNRAS, 439, 690
Huang, J., Luo, B., Du, P., et al. 2020, ApJ, 895, 114
Ighina, L., Caccianiga, A., Moretti, A., et al. 2019, MNRAS, 489, 2732
Ighina, L., Caccianiga, A., Moretti, A., et al. 2023, MNRAS, 519, 2060
Ighina, L., Caccianiga, A., Moretti, A., et al. 2024, A&A, 687, A242
Ighina, L., Caccianiga, A., Moretti, A., et al. 2025, A&A, 698, A158
Ighina, L., Moretti, A., Tavecchio, F., et al. 2022, A&A, 659, A93
Inayoshi, K., Kimura, S. S., & Noda, H. 2024, arXiv:2412.03653
Jolley, E. J. D., & Kuncic, Z. 2008, MNRAS, 386, 989
Kale, R., & Ishwara-Chandra, C. H. 2021, ExA, 51, 95
Kara, E., Garcìa, J. A., Lohfink, A., et al. 2017, MNRAS, 468, 3489
Khorunzhev, G. A., Meshcheryakov, A. V., Medvedev, P. S., et al. 2021, AstL, 47, 123
King, A. 2024, MNRAS, 531, 550
Konigl, A. 1981, ApJ, 243, 700
Lambrides, E., Garofali, K., Larson, R., et al. 2024, arXiv:2409.13047
Latif, M. A., Whalen, D. J., Khochfar, S., Herrington, N. P., & Woods, T. E. 2022, Natur, 607, 48
Laurenti, M., Piconcelli, E., Zappacosta, L., et al. 2022, A&A, 657, A57
Li, J.-T., Wang, F., Yang, J., et al. 2021, ApJ, 906, 135
Liu, H., Luo, B., Brandt, W. N., et al. 2021, ApJ, 910, 103
Liuzzo, E., Giroletti, M., Giovannini, G., et al. 2013, A&A, 560, A23
Lupi, A., Haiman, Z., & Volonteri, M. 2021, MNRAS, 503, 5046
Lupi, A., Quadri, G., Volonteri, M., Colpi, M., & Regan, J. A. 2024a, A&A, 686, A256
Lupi, A., Trinca, A., Volonteri, M., Dotti, M., & Mazzucchelli, C. 2024b, A&A, 689, A128
Lusso, E., & Risaliti, G. 2016, ApJ, 819, 154
Madau, P. 2025, arXiv:2501.09854
Madau, P., & Haardt, F. 2024, ApJL, 976, L24
Maiolino, R., Risaliti, G., Signorini, M., et al. 2025, MNRAS, 538, 1921
Maiolino, R., Scholtz, J., Witstok, J., et al. 2024, Natur, 627, 59
Marcotulli, L., Connor, T., Bañados, E., et al. 2025, ApJL, 979, L6
Massaro, E., Perri, M., Giommi, P., & Nesci, R. 2004, A&A, 413, 489
Massonneau, W., Volonteri, M., Dubois, Y., & Beckmann, R. S. 2023, A&A, 670, A180
Matsuoka, Y., Iwasawa, K., Onoue, M., et al. 2018, ApJS, 237, 5
Mazzucchelli, C., Bischetti, M., D'Odorico, V., et al. 2023, A&A, 676, A71
McConnell, D., Hale, C. L., Lenc, E., et al. 2020, PASA, 37, e048
McMullin, J. P., Waters, B., Schiebel, D., Young, W., & Golap, K. 2007, in ASP Conf. Ser. 376 ADASS XVI (San Francisco, CA: ASP), 127
Medvedev, P., Gilfanov, M., Sazonov, S., Schartel, N., & Sunyaev, R. 2021, MNRAS, 504, 576
Medvedev, P., Sazonov, S., Gilfanov, M., et al. 2020, MNRAS, 497, 1842
Meier, D. L. 2002, NewAR, 46, 247
Middei, R., Giommi, P., Perri, M., et al. 2022, MNRAS, 514, 3179
Migliori, G., Siemiginowska, A., Sobolewska, M., et al. 2023, MNRAS, 524, 1087
Moretti, A., Ballo, L., Braito, V., et al. 2014, A&A, 563, A46

---

[25] Considering Fermi-LAT sensitivity at high galactic latitude ($|b| > 45°$) and an energy of 1 GeV, as described in https://www.slac.stanford.edu/exp/glast/groups/canda/lat_Performance.htm.

Moretti, A., Ghisellini, G., Caccianiga, A., et al. 2021, ApJ, 920, 15
Murphy, T., Chatterjee, S., Kaplan, D. L., et al. 2013, PASA, 30, e006
Murphy, T., Kaplan, D. L., Stewart, A. J., et al. 2021, PASA, 38, e054
Nanni, R., Vignali, C., Gilli, R., Moretti, A., & Brandt, W. N. 2017, A&A, 603, A128
Pacucci, F., & Narayan, R. 2024, ApJ, 976, 96
Paliya, V. S., Ajello, M., Cao, H. M., et al. 2020a, ApJ, 897, 177
Paliya, V. S., Domínguez, A., Cabello, C., et al. 2020b, ApJL, 903, L8
Piner, B. G., Pant, N., & Edwards, P. G. 2010, ApJ, 723, 1150
Pognan, Q., Trakhtenbrot, B., Sbarrato, T., Schawinski, K., & Bertemes, C. 2020, MNRAS, 492, 4058
Polletta, M., Tajer, M., Maraschi, L., et al. 2007, ApJ, 663, 81
Reddy, S. H., Kudale, S., Gokhale, U., et al. 2017, JAI, 6, 1641011
Reynolds, J. 1994, ATNF Technical Memos, 39.3/040
Ricarte, A., Narayan, R., & Curd, B. 2023, ApJL, 954, L22
Rigamonti, F., Severgnini, P., Sottocorno, E., et al. 2025, A&A, 693, A117
Risaliti, G., Young, M., & Elvis, M. 2009, ApJL, 700, L6
Ross, K., Hurley-Walker, N., Galvin, T. J., et al. 2024, PASA, 41, e054
Sault, R. J., Teuben, P. J., & Wright, M. C. H. 1995, in ASP Conf. Ser. 77 ADASS IV, ed. R. A. Shaw, H. E. Payne, & J. J. E. Hayes (San Francisco, CA: ASP), 433
Savić, D. V., Hutsemékers, D., & Sluse, D. 2024, A&A, 687, A114
Schauer, A. T. P., Regan, J., Glover, S. C. O., & Klessen, R. S. 2017, MNRAS, 471, 4878
Shaban, F., Siemiginowska, A., Suleiman, R. M., El-Nawawy, M. S., & Ali, A. 2022, JHEAp, 36, 152
Shemmer, O., Brandt, W. N., Netzer, H., Maiolino, R., & Kaspi, S. 2008, ApJ, 682, 81
Shemmer, O., Brandt, W. N., Paolillo, M., et al. 2014, ApJ, 783, 116
Shemmer, O., Brandt, W. N., Vignali, C., et al. 2005, ApJ, 630, 729
Shen, X., Hopkins, P. F., Faucher-Giguère, C.-A., et al. 2020, MNRAS, 495, 3252
Shen, Y., Wu, J., Jiang, L., et al. 2019, ApJ, 873, 35
Spingola, C., Dallacasa, D., Belladitta, S., et al. 2020, A&A, 643, L12
Suh, H., Scharwächter, J., Farina, E. P., et al. 2025, NatAs, 9, 271
Tortosa, A., Ricci, C., Tombesi, F., et al. 2022, MNRAS, 509, 3599
Tortosa, A., Zappacosta, L., Piconcelli, E., et al. 2024, A&A, 691, A235
Vignali, C., Brandt, W. N., Schneider, D. P., Kaspi, S., et al. 2005, AJ, 129, 2519
Vito, F., Brandt, W. N., Bauer, F. E., et al. 2019, A&A, 630, A118
Volonteri, M., & Begelman, M. C. 2010, MNRAS, 409, 1022
Volonteri, M., Habouzit, M., & Colpi, M. 2021, NatRP, 3, 732
Wachter, K., Leach, R., & Kellogg, E. 1979, ApJ, 230, 274
Wang, F., Fan, X., Yang, J., et al. 2021a, ApJ, 908, 53
Wang, F., Yang, J., Fan, X., et al. 2021b, ApJL, 907, L1
Wells, D. C. 1985, in Data Analysis in Astronomy, Proc. of the 1st Workshop held in Erice, ed. V. Di Gesù et al. (New York: Plenum Press), 195
Wierzcholska, A., & Wagner, S. 2025, A&A, 693, A299
Willott, C. J., Delorme, P., Reylé, C., et al. 2010, AJ, 139, 906
Wilson, W. E., Ferris, R. H., Axtens, P., et al. 2011, MNRAS, 416, 832
Wolf, J., Nandra, K., Salvato, M., et al. 2023, A&A, 669, A127
Wu, X.-B., Wang, F., Fan, X., et al. 2015, Natur, 518, 512
Wu, Z., Jiang, D. R., Gu, M., & Liu, Y. 2007, A&A, 466, 63
Yang, J., Wang, F., Fan, X., et al. 2021, ApJ, 923, 262
Yue, M., Eilers, A.-C., Ananna, T. T., et al. 2024, ApJL, 974, L26
Zappacosta, L., Piconcelli, E., Fiore, F., et al. 2023, A&A, 678, A201
Zhang, Y.-H., & Li, J.-C. 2017, MNRAS, 469, 1682
Zuo, Z., Zhu, S., Brandt, W. N., et al. 2024, MNRAS, 530, 360